Transverse asymmetry in molecular strong-field photoelectron holography induced by initial phase structure and Coulomb field

Long Xu,[1,*] Peng Qin,[1,*] Min Gong,[1] Wen She,[1] Lingling Zheng,[2,†] Xufei Sun,[1,‡] and Zhanghai Chen[1,§]
[1]*Department of Physics, Xiamen University, Xiamen 361005, China*
[2]*School of Energy Research, Xiang'an Campus, Xiamen University, Xiamen 361100, China*

(Received 18 March 2024; revised 26 May 2024; accepted 11 June 2024; published 1 July 2024)

Transverse asymmetry (TA) signifies a feature of the photoelectron momentum distribution (PMD) when linearly polarized light interacts with tilted molecules, which has been widely employed in strong-field photoelectron holography. The initial phase structure and the asymmetric Coulomb field are considered as two different physical origins for the TA. Through the molecular quantum trajectory Monte Carlo method, we correct some misconceptions in previous studies and refine the physical picture regarding how these two factors modulate TA in PMDs. We demonstrate the critical influence of the multiple-constituent atomic orbitals for ionizing the molecular orbital on the initial phase structure. This phase structure introduces an additional phase difference between tunneling electrons, leading to the rotation of the spiderlike and comblike fringes while maintaining the structure of the above-threshold ionization rings. In contrast, the asymmetric Coulomb field modulates the amplitude distribution of tunneling electrons depending on the tunneling sites, resulting in changes in the intensity of the fringes. Additionally, apart from the TA signal induced by the asymmetric Coulomb field for the indirect electrons, we also identified the reverse TA signal for the direct ones near zero momentum.

DOI: 10.1103/PhysRevA.110.013105

I. INTRODUCTION

Electron holography provides powerful technical support for the three-dimensional electron microscopic image of microscopic matter. Utilizing the wave nature of electrons, the scattered and nonscattered parts of the electron wave packet (EWP) are overlapped to generate a stripy interference pattern—the hologram. In the past 20 years, strong-field photoelectron holography (SFPH) has been understood and widely used in strong-field physics. Here, the typical hologram [1] is produced by the interference of two kinds of EWP in the photoelectron momentum distribution (PMD). One involves electrons flying directly to the detector after tunneling ionization, serving as the reference wave, which encodes the information of the initial state; the other involves ionized electrons that may return and scatter off the parent ion, regarded as the signal wave, which contains the information of the scattering core. As a result, SFPH holds the unique potential for probing the temporal and structural properties of atomic and molecular systems with angstrom and attosecond precision [2–9]. It has been reported that the photoemission position was experimentally measured in the ionization of atoms with SFPH [5], timing in photoionization can be retrieved based on SFPH [2,3], and the attosecond migration of the valence electron in molecules is directly visualized by applying the SFPH [7].

Meckel *et al.* first reported in experiment that the holograms depend on the molecular alignment [10]. When a linearly polarized laser field interacts with a molecule that is tilted against the laser polarization direction, a tiny shift is observed in the interference pattern, resulting in a transverse asymmetry (TA) perpendicular to the polarization axis. They revealed that this shift is caused by a transverse displacement of the EWP in the position space immediately after tunneling. Tan *et al.* further retrieved this transverse emission position in terms of SFPH [11]. Actually, this transverse displacement in the position space corresponds to an additional phase structure of the continuous electron in the momentum space [12] and Liu *et al.* extracted this additional initial phase of the tunneling EWP from the transition amplitude within the strong-field approximation [13,14].

Recently, Ortmann *et al.* further point out that the asymmetric Coulomb field of tilted molecules also has influence on the TA of the holographic interference pattern [15]. For molecules, there are several tunneling sites. The EWP may undergo adiabatic relaxation to the atoms with the lowest potential energy before ionization. Alternatively, it may directly ionize from atoms with higher potential energy, a phenomenon known as enhanced ionization [16–28]. It is shown that electrons that tunnel from different sites, i.e., up- or down-field atoms, will undergo a different degree of deflection because of the asymmetric Coulomb field, ultimately leading to a TA in the interference pattern as well. Taking advantage of this feature, they further estimate the ratio of electrons born from the up- and down-field atoms [15].

The alignment-dependent PMDs measured experimentally have been quantitatively reproduced in simulations considering these two factors, but some contradictions and unclear

*These authors contributed equally to this work.
†Contact author: llzheng@xmu.edu.cn
‡Contact author: xfsun@xmu.edu.cn
§Contact author: zhanghai@xmu.edu.cn

points still remain. A long-standing contradiction is that the bond length of N_2 in the model needed to be set to 4 a.u. rather than the equilibrium bond length of 2.07 a.u. to reproduce the experimental measurements [10,13]. Additionally, although both the initial phase structure and the asymmetric Coulomb field can give rise to TA, and they are both essentially caused by the spatial offset of the EWP emission position from the geometric center of the molecule, is there a fundamental distinction between the "spatial offset-induced initial phase structure" and the "spatial offset-induced asymmetric Coulomb field" in their manifestations in the alignment-dependent PMDs? If there is, how do they induce TA in PMDs, respectively?

In this study, we employ a molecular quantum trajectory Monte Carlo (MO-QTMC) model to investigate the mechanisms responsible for generating TA due to the initial phase structure and the asymmetric Coulomb field, respectively. By combining $2s$ and $2p_z$ atomic orbitals to more accurately mimic the $3\sigma_g$ highest occupied molecular orbit (HOMO) of N_2, we reproduce the experimentally measured alignment-dependent PMDs [10] at an equilibrium bond length of 2.07 a.u. We further show that the initial phase structure induces interference fringe shift, varying for different interference patterns, while the asymmetric Coulomb field modulates the intensity of the fringes. Additionally, we identified TA signals from direct electrons near zero momentum that were overlooked in earlier studies.

The paper's structure is outlined as follows: Section II introduces the MO-QTMC model utilized in this study and describes the data processing techniques. In Sec. III A, we elucidate the role of the initial phase structure in generating TA. Section III B explains how the asymmetric Coulomb field contributes to TA. The abbreviation a.u. throughout the paper denotes atomic units.

II. THE SEMICLASSICAL MODEL

We perform the MO-QTMC [13] simulation to study the TA of N_2 molecules in strong laser fields. The MO-QTMC model is improved from the atomic QTMC model [29,30] after considering the molecular orbital effect [31,32]. In the simulation, the determination of the tunneling site involves two approaches: one is given by the Landau effective theory [33]; the other builds upon the former but introducing a spatial offset from the geometric center of the molecule. This offset accounts for the transverse displacement in position space associated with the up- and down-field tunneling [15]. The tunneled electron carries a Gaussian-like transverse momentum distribution perpendicular to the instantaneous electric field and zero longitudinal momentum along the field. The ionization probability of tunneled electrons is given by the modified Ammosov-Delone-Krainov (ADK) theory [13,29,34] and includes the correction induced by the molecular alignment and bond length [13]. After tunneling, based on Feynman's path integral approach, the evolution of EWP in combined laser and Coulomb field can be represented by quantum trajectories. The electron motion is determined by the classical Newtonian equation,

$$\ddot{\mathbf{r}} = -\nabla V(\mathbf{r}) - \mathbf{E}(t), \tag{1}$$

where $\mathbf{E}(t)$ is the electric field and $V(\mathbf{r}) = -\sum_{J=1}^{2} Z_J(\mathbf{r}-\mathbf{R}_J)/\sqrt{|\mathbf{r}-\mathbf{R}_J|^2+a^2}$ is the one-electron soft-core potential, as in Ref. [35]. Here, $Z_J(\mathbf{r}-\mathbf{R}_J) = Z_J^{\infty} + (Z_J^0 - Z_J^{\infty})\exp(-|\mathbf{r}-\mathbf{R}_J|^2/\sigma^2)$ is the position-dependent effective charge. J labels the nuclei at fixed positions $\mathbf{R}_J = (-1)^J\mathbf{R}_0/2$, where R_0 is the bond length. For N_2, the bare charge parameter $Z_J^{\infty} = 0.5$, and the effective nuclear charge $Z_J^0 = 7$. Soft-core parameters $a = 1.2$ and effective charge shielding parameter $\sigma = 0.836$ are chosen to match the ionization potential of N_2's HOMO.

The phase of each quantum trajectory is calculated by the phase equation $S = \phi_{\text{pro}} + \phi_{\text{ini}}$. Here,

$$\phi_{\text{pro}} = -\int_{t_r}^{T_p} [\mathbf{v}(t)^2/2 + V[\mathbf{r}(t)] - \mathbf{r}(t)\cdot\nabla V[\mathbf{r}(t)] + I_p]\mathrm{d}t \tag{2}$$

is the phase accumulated during propagation [30,36], where I_p is the binding energy. ϕ_{ini} represents the initial phase, which can be extracted from the ionizing molecular orbital. Since $2s$ and $2p_z$ orbitals mainly contribute to the $3\sigma_g$ HOMO in N_2 [37,38], different from the previous study where $1s$ orbitals are used [13], we combine $2s$ and $2p_z$ orbitals to mimic the $3\sigma_g$ HOMO more accurately. The structural factor S_{MO}, dependent on the HOMO, is given by

$$S_{\text{MO}} = C_{(2s)3\sigma_g} S_{(2s)3\sigma_g} + C_{(2p_z)3\sigma_g} S_{(2p_z)3\sigma_g}. \tag{3}$$

$S_{(2s)3\sigma_g}$ and $S_{(2p_z)3\sigma_g}$ are the structural factors corresponding to the bonding combination of $2s$ and $2p_z$ orbitals with the weighted coefficients of $C_{(2s)3\sigma_g}$ and $C_{(2p_z)3\sigma_g}$ respectively. The respective structural factors can be written as follows:

$$S_{(2s)3\sigma_g} = -\frac{2\kappa_n^{9/2}}{\pi\sqrt{1+S_{2s}(R_0)}}\cos\left\{\frac{v_{y0}R_0\sin(\theta)}{2} - \frac{i\mathrm{sgn}[E(t_r)]\sqrt{2\mathrm{I_p}+v_{y0}^2}R_0\cos(\theta)}{2}\right\} \tag{4}$$

and

$$S_{(2p_z)3\sigma_g} = -\frac{2\kappa_n^{7/2}}{\pi\sqrt{1-S_{2p_z}(R_0)}}\sin\left\{\frac{v_{y0}R_0\sin(\theta)}{2} - \frac{i\mathrm{sgn}[E(t_r)]\sqrt{2\mathrm{I_p}+v_{y0}^2}R_0\cos(\theta)}{2}\right\}$$
$$\times\left\{v_{y0}\sin(\theta) - i\mathrm{sgn}[E(t_r)]\sqrt{2I_p+v_{y0}^2}\cos(\theta)\right\}. \tag{5}$$

Here, $k_n^2 = 2I_p$. $S_{2s}(R_0)$ and $S_{2p_z}(R_0)$ are the respective atomic orbital overlap integrals. v_{y0} represents the initial transverse momentum. θ represents the angle of molecular alignment. t_r is the real part of electron birth time and $\mathrm{sgn}[E(t_r)]$ represents the direction of the instantaneous electric field. The detailed derivation can be found in Sec. II of the Supplemental Material [39]. Based on the relation $S_{\mathrm{MO}} = ae^{i\phi_{\mathrm{ini}}}$, we obtain the initial phase structure $\phi_{\mathrm{ini}} = \arctan(\mathrm{Im}[S_{\mathrm{MO}}]/\mathrm{Re}[S_{\mathrm{MO}}])$. Finally, those different quantum trajectories will interfere with each other when they have the same asymptotic momentum.

In the simulation, neutral N_2 molecules with a valence $3\sigma_g$ shell are ionized by the laser pulse polarized along the x axis. The N_2 molecules are aligned in the xy plane and tilted at an angle with respect to the laser polarization axis that can induce TA in the PMDs. The laser pulse with a cosine waveform has a wavelength of 800 nm, a peak intensity of $I_1 = 1.3 \times 10^{14}$ W/cm^2, and a duration of six cycles with a constant amplitude for the first four cycles and a two-cycle ramp at the end.

Although the PMDs can intuitively exhibit the asymmetrical distribution, it is hard to quantify the degree of TA. To address this, we extract the average of the transverse momentum v_y for each momentum v_x, as in Ref. [15]:

$$v_{y,\mathrm{mean}}[v_x(i)] = \frac{\sum_{j=1}^{n} w(i,j)v_y(j)}{\sum_{j=1}^{n} w(i,j)}, \tag{6}$$

where $w(i, j)$ represents the PMD in the ith and jth bins of the histogram along v_x and v_y, respectively.

III. RESULTS AND DICUSSIONS

A. The initial phase structure

Although the alignment-dependent PMDs measured experimentally have been quantitatively reproduced in both the quantum model of the time-dependent Schrödinger equation [10] and the semiclassical QTMC model [13], a puzzling contradiction persists in these simulations. Specifically, the bond length of N_2 needs to be set to 4 a.u. rather than the equilibrium bond length of 2.07 a.u. In previous models, a $(1s)3\sigma_g$ orbital was utilized to mimic the HOMO of N_2. However, as we know, such an approximation is overly simplistic, because the HOMO should be expanded into multiple constituent atomic orbitals. To address the contradiction, we combine $2s$ and $2p_z$ orbitals $[(2s2p_z)3\sigma_g]$ to more accurately mimic the $3\sigma_g$ HOMO of N_2 (see Sec. I of the Supplemental Material [39] for details on the approximation of the HOMO). We follow Refs. [10,13] to calculate the normalized difference (ND) plots defined as $\mathrm{ND} = [D(\mathbf{p},\theta) - D_{\mathrm{ref}}(\mathbf{p})]/[D(\mathbf{p},\theta) + D_{\mathrm{ref}}(\mathbf{p})]$, where $D(\mathbf{p},\theta)$ represents the PMDs corresponding to the alignment angle θ, and $D_{\mathrm{ref}}(\mathbf{p})$ is the reference which is the sum PMD over all PMDs for alignment angles from 0° to 180° in 2° increments. Both $D(\mathbf{p},\theta)$ and $D_{\mathrm{ref}}(\mathbf{p})$ are normalized. For each angle, considering the influence of the focal volume effect, we calculate 12 intensities in the range $(0.7-1.3) \times 10^{14}$ W/cm^2. The relative weight of each intensity is given by $\mathrm{dVol}/\mathrm{d}I \propto (I_0 + 2I)\sqrt{I_0 - I}/I^{5/2}$ [44].

In Figs. 1(a), 1(b), and 1(c), we show the ND plots at the alignment angles 0°, 45°, and 90°, respectively. For 0° and 90°, the difference PMDs are symmetric with respect to the laser polarization. But for 45°, the distinctive TA manifests in the ND plot. Our results perfectly agree with the experimental measurement [10] under consideration of the equilibrium bond length of N_2. It is interesting that either stretching the bond length of $(1s)3\sigma_g$ to 4 a.u. or combining $2s$ and $2p_z$ orbitals to mimic the HOMO can successfully replicate the experimental measurements.

To further understand the mechanism behind this outcome, we show the initial phase structure for different molecular orbitals separately in Fig. 1(d). For the bonding combination of pure $1s$ orbitals $[(1s)3\sigma_g]$ as depicted by the blue (dark gray) line, the initial phase changes very slowly with the initial transverse momentum at the equilibrium bond length $R_0 = 2.07$ a.u., and thus it is difficult to observe TA in PMDs. The initial phase structure in momentum space essentially corresponds to the transverse displacement of tunneling electrons in position space, linked by Fourier transformation [12]. The greater the spatial offset, the more rapid the changes of the initial phase with the initial transverse momentum will be. In Fig. 1(d), it is evident that the slope increases with the stretching of the bond length, as seen by the blue (dark gray) and orange (medium gray) lines. Therefore, the TA can be more readily observed at the bond length $R_0 = 4$ a.u. On the other hand, one can find the comparable initial phase structure extracted from $(2s2p_z)3\sigma_g$ at the equilibrium bond length and from $(1s)3\sigma_g$ at the bond length of 4 a.u., as depicted by the yellow (light gray) and orange (medium gray) lines. This can be intuitively understood from the shape of the orbital. For $(2s2p_z)3\sigma_g$, p_z orbitals have a dumbbell shape with two lobes aligned along molecular axes. These lobes extend farther away from the nucleus compared to the spherical distribution of s orbitals. In other words, the involvement of p_z orbitals leads to the larger spatial distribution. That is the reason why the overly simplified $(1s)3\sigma_g$ had to be stretched to reproduce experimental measurements. Thus, the weighted coefficients of the constituent atomic orbitals for the ionizing molecular orbital have a critical effect on the initial phase structure.

When the initial phase structure is introduced into the model, we can reproduce the experimentally observed tiny shift of interference fringes. The initial phase structure represents the phase distortions of the EWP at the tunneling exit. The interference fringes reflect the phase differences between subwaves of the EWP. However, we still lack a clear physical picture of how the initial phase structure modifies the phase differences, thereby affecting the interference fringes. Both the initial phase structure ϕ_{ini} and the asymmetric Coulomb field can cause TA, and they are always considered together in the QTMC simulations to replicate the experimental results [13,15]. To investigate the ϕ_{ini} effect on TA of interference patterns, we first need to rule out the influence of the asymmetric Coulomb field. This can be easily achieved by disregarding the impact of the Coulomb field in the electron propagation process. However, once the Coulomb factor is turned off, the interference structure associated with the rescattering EWP will disappear. Considering that the wavelength of the scattered electron after tunneling is too long to effectively resolve the bond length of N_2 in equilibrium

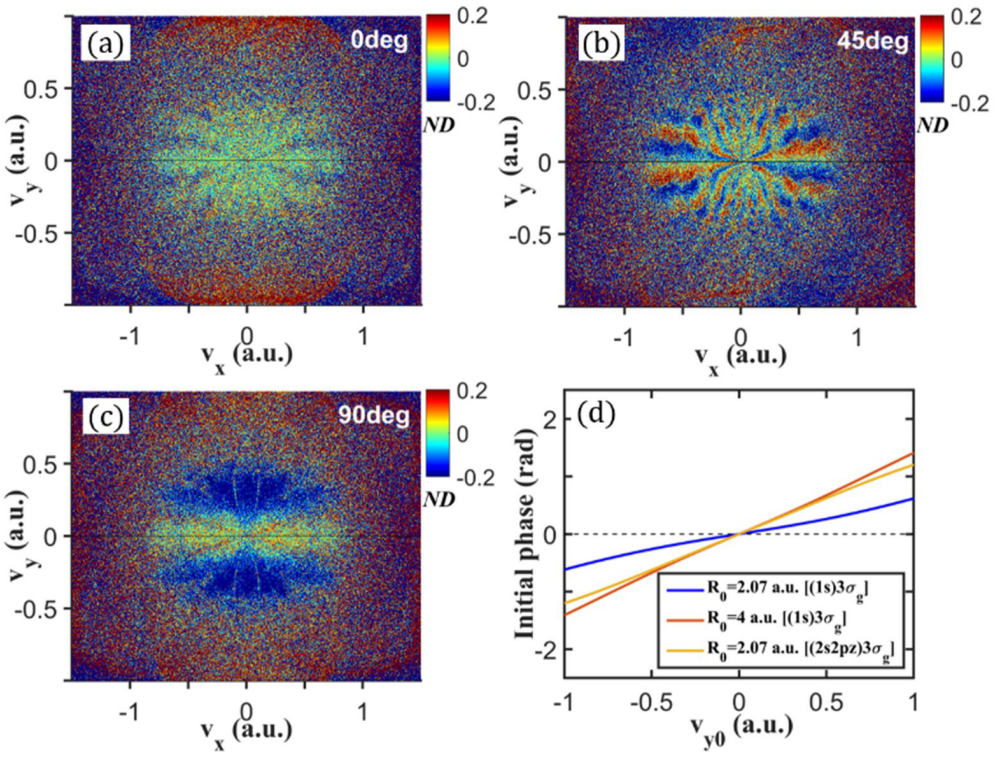

FIG. 1. The normalized difference (ND) plots of N_2 molecules at the alignment angle of (a) 0°, (b) 45°, and (c) 90°. (d) The initial phase ϕ_{ini} as a function of the initial transverse momentum v_{y0} for different molecular orbitals at an alignment of 45°. The blue (dark gray) and orange (medium gray) curves correspond to the $(1s)3\sigma_g$ HOMO at bond lengths of 2.07 and 4 a.u., respectively. The yellow (light gray) curve corresponds to the $(2s2p_z)3\sigma_g$ HOMO at the bond length of 2.07 a.u.

under the laser parameters we utilized [10], we modify the molecular potential to an equivalent atomic potential, i.e., $V_a(\mathbf{r}) = -\sum_{J=1}^{2} \frac{Z_J^{\infty}+(Z_J^0-Z_J^{\infty})\exp(-|\mathbf{r}|^2/\sigma^2)}{\sqrt{|\mathbf{r}|^2+a^2}}$, to neglect TA caused by the asymmetric Coulomb field but still retain the role of the symmetric Coulomb field in the electron motion.

Figures 2(a) and 2(b) show the simulated PMD and the corresponding $v_{y,\text{mean}}$ curve [the blue (dark gray) line] from N_2 molecules tilted 45° against the laser polarization, respectively. It is obvious that the spiderlike fringes are tilted, and they exhibit an asymmetric distribution about $v_y = 0$. The $v_{y,\text{mean}}$ curve calculated by the classical-trajectory Monte Carlo (CTMC) model is also shown in Fig. 2(b) as the yellow (light gray) line. In comparison to the QTMC result, this curve is obtained without phase structure ($\phi_{\text{ini}} + \phi_{\text{pro}}$) included. One can clearly identify that it is transversely symmetrical without any momentum offset. By replacing molecular potential with $V_a(\mathbf{r})$, thus, the asymmetric Coulomb field-induced TA can be totally suppressed and the initial phase-induced TA is isolated.

The phase-dependent $v_{y,\text{mean}}$ curve in Fig. 2(b) exhibits a three-stage structure: an oscillatory plateau for $|v_x| < 0.5$ and two steep slopes for $|v_x| > 0.5$. Although it generally presents a positive slope distribution as well, this segmented structure is still different from the previously reported result with a smooth slope distribution [15]. Taking a careful comparison between the PMD and the $v_{y,\text{mean}}$ curve, one can find that the location of the curve inflection point, $v_x \approx |0.5|$, is where the spiderlike fringes begin to dominate among the various interference structures.

To understand this unique $v_{y,\text{mean}}$ curve structure, we separate several typical interference patterns, i.e., the spiderlike fringes [1,45], the above-threshold ionization (ATI) rings [46–48], and the comblike intracycle fringes [46], by constraining the birth time of electrons, as illustrated in Figs. 3(a), 3(c), and 3(e) respectively. Due to the central symmetry of the PMD, here we only show the results with positive v_x. Different interference structures exhibit distinct $v_{y,\text{mean}}$ curves. For the curve extracted from the spider, as shown in Fig. 3(b), it has a smooth positive slope with a positive $v_{y,\text{mean}}$, which means the spiderlike fringes in Fig. 3(a) rotate anticlockwise as indicated by the white arrows. The curve for the ATI rings in Fig. 3(d) exhibits a nearly zero slope located at $v_{y,\text{mean}} = 0$, which makes it seem that ϕ_{ini} has a negligible effect on it. Regarding the comblike fringes, the extracted curve in Fig. 3(f) exhibits an oscillating distribution centered around each vertical stripe in Fig. 3(e), indicating a rotation of each comb fringe. One can easily identify that the segmented $v_{y,\text{mean}}$ curve structure in Fig. 2(b) comes from the combined effect of $v_{y,\text{mean}}$ curve distribution across all interference structures. However, the mechanism responsible for distinct shift effects observed in various interference fringes caused by the initial phase is still hidden.

It is useful to recall that the primary factor contributing to the phase difference in the spiderlike fringes is [1]

$$\Delta\phi = \phi_{\text{signal}} - \phi_{\text{ref}} \approx \frac{v_y^2\left(t_C - t_0^{\text{ref}}\right)}{2}. \tag{7}$$

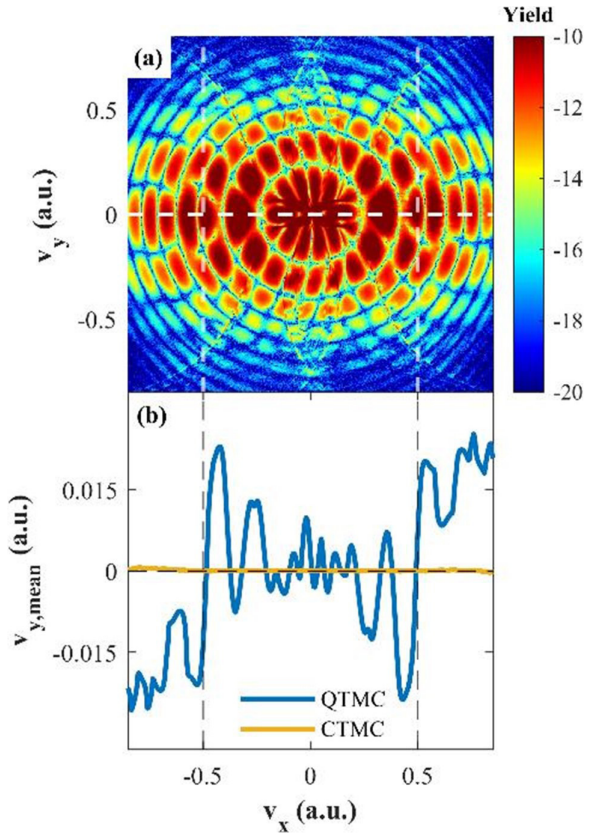

FIG. 2. (a) The PMD of N_2 molecules at an alignment angle of 45°. The molecular potential is modified to an equivalent atomic potential to ignore the TA caused by the asymmetric Coulomb field. (b) The extracted $v_{y,\mathrm{mean}}$ as a function of v_x. The blue (dark gray) curve is obtained through QTMC simulation, while the yellow (light gray) curve is obtained by CTMC simulation without the inclusion of the phase structure. Interference pattern is plotted in logarithmic color scale.

Here, t_0^{ref} is the ionization time of the reference wave and t_C is the collision time of the signal wave. They manifest clear counterparts of quantum trajectories in the semiclassical model. The reference wave corresponds to the indirect electrons, while the signal wave corresponds to the forward-scattered electrons [49]. They depart from the same tunneling site, which is on the opposite side of the detector, but with the difference that the transverse momentum changes sign for the forward-scattered electrons (i.e., $v_{y0} \times v_y < 0$), while it remains in the same direction for the indirect ones (i.e., $v_{y0} \times v_y > 0$). Since the ϕ_{ini} has a linear dependence on the initial transverse momentum v_{y0}, as shown in Fig. 3(g), an additional initial phase difference is introduced between indirect and forward-scattered electrons with the same final momentum:

$$\Delta\phi_{\mathrm{ini-spider}} = \phi_{\mathrm{ini}}(v_{y0,\mathrm{forward}}) - \phi_{\mathrm{ini}}(v_{y0,\mathrm{indirect}}). \quad (8)$$

Here $\mathrm{sgn}(v_{y0,\mathrm{forward}}) = -\mathrm{sgn}(v_{y0,\mathrm{indirect}})$, where $v_{y0,\mathrm{indirect}}$ and $v_{y0,\mathrm{forward}}$ represent the v_{y0} of indirect and forward-scattered electrons, respectively. Combining the aforementioned relationship between v_{y0} and v_y of indirect and forward-scattered electrons, therefore, this additional phase difference depends on the final momentum v_y as follows:

$$\Delta\phi_{\mathrm{ini-spider}} < 0, \text{ for } v_y > 0 \text{ and } \Delta\phi_{\mathrm{ini-spider}} > 0, \text{ for } v_y < 0. \quad (9)$$

Consequently, $\Delta\phi_{\mathrm{ini-spider}}$ manifests as a counterclockwise rotation of spiderlike fringes in the momentum spectrum.

As for ATI rings, they arise from the interference of electrons born in different cycles with the same type, i.e., both direct, indirect, or scattered ones. For energies below $2U_p$, the dominance of ATI rings is attributed to the contribution from the direct ones. Since the phase difference $\Delta\phi_{\mathrm{ini-ATI}}$ introduced between direct electrons with identical v_{y0} is approximately zero, its ϕ_{ini}-induced shift in the PMD is too negligible to be observed in Fig. 3(c).

The comblike fringes result from the superposition between the indirect and direct electrons. They depart from two different tunneling sites, which are on either side of the parent ion, with the same v_{y0}. Despite their identical v_{y0}, the comblike fringes are modulated significantly by the initial phase, which deviates from the behavior observed in the ATI rings. In other words, there is an additional nonzero initial phase difference, $\Delta\phi_{\mathrm{ini-comb}}=\phi_{\mathrm{indirect}}-\phi_{\mathrm{direct}}$, introduced between them. This comes from the fact that the initial phase depends not only on the v_{y0} but also on the direction of the electric field at the electron birth time, as shown in Fig. 3(g). The ϕ_{ini} has a positive linear dependence on the initial transverse momentum v_{y0} for $E(t) > 0$, while it has a negative linear dependence for $E(t) < 0$. Despite these two types of coherent electrons having the same v_{y0}, the direction of the electric field at their birth time is different. As a result, this additional phase difference,

$$\Delta\phi_{\mathrm{ini-comb}} < 0, \text{ for } v_y > 0 \text{ and } \Delta\phi_{\mathrm{ini-comb}} > 0, \text{ for } v_y < 0, \quad (10)$$

leads to a counterclockwise rotation of each comblike fringe and an oscillatory distribution of the whole $v_{y,\mathrm{mean}}$ curve.

To put it briefly, rather than the absolute value of the initial phase, its dependence on the initial transverse momentum v_{y0} and the direction of the electric field at the tunneling exit is more noteworthy. The initial phase structure introduces an additional initial phase difference between electron trajectories, leading to the rotation of the spiderlike and comblike fringes while maintaining the structure of the ATI rings.

B. The asymmetric Coulomb field

Besides the initial phase structure, the asymmetric Coulomb field can also give rise to TA. The mechanism behind the asymmetric Coulomb-field-induced TA and its impact on interference fringes in momentum space remain unclear. To systematically investigate the effect of the asymmetric Coulomb field in isolation, we first need to eliminate the influence of ϕ_{ini}. In the MO-QTMC model, ϕ_{ini} and the transversely asymmetric Coulomb field are mutually independent. Therefore, the influence of the initial phase structure can be easily eliminated by setting ϕ_{ini} to zero. In addition, various interference structures in PMD may interfere with the accurate extraction of $v_{y,\mathrm{mean}}$ curves caused only by the asymmetric Coulomb field. To eliminate these oscillating background signals superimposed on the $v_{y,\mathrm{mean}}$ curve, here we further ignore the propagation phase ϕ_{pro} of the EWP.

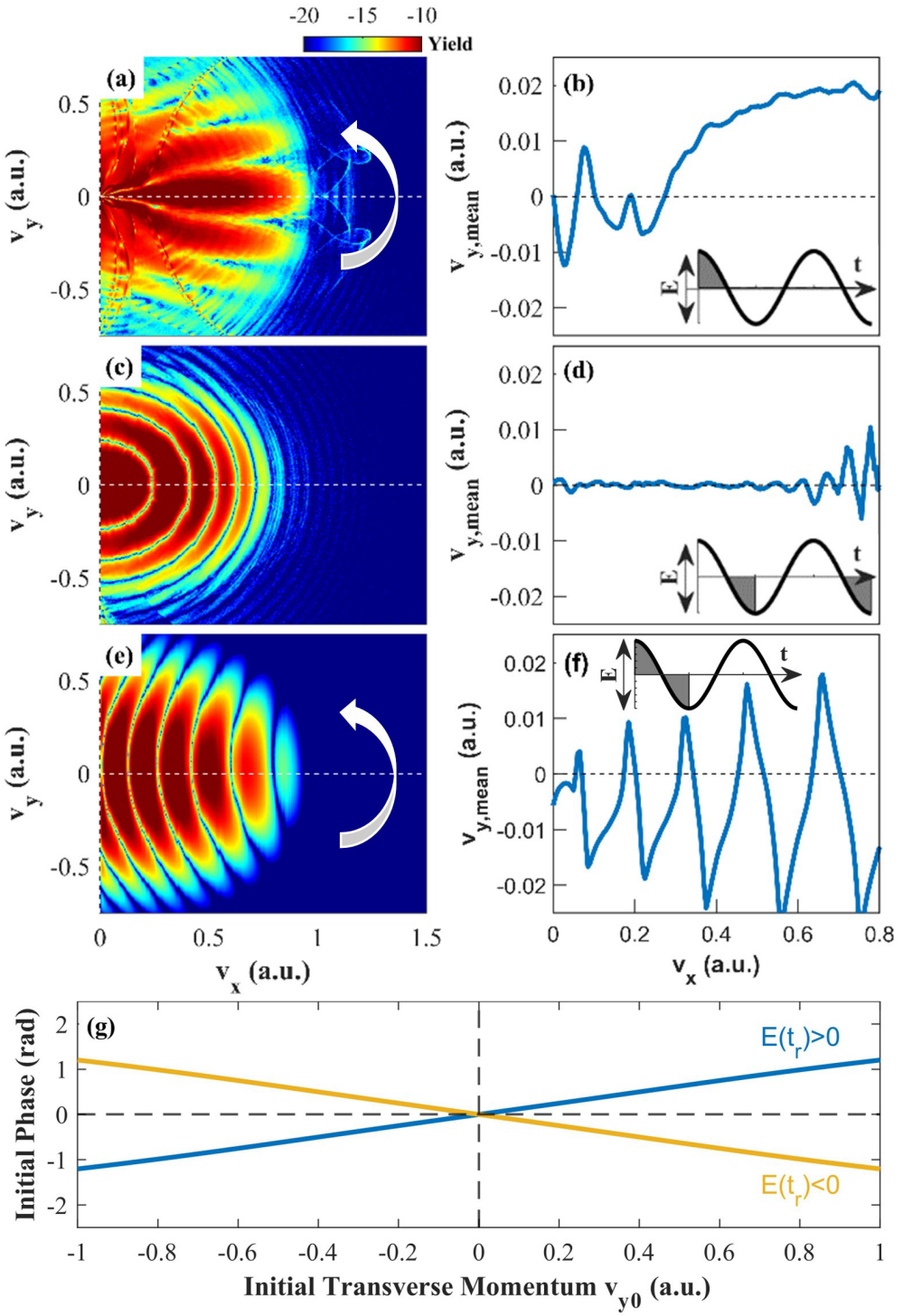

FIG. 3. Separated interference patterns from Fig. 2(a) by constraining the birth time of electrons: (a) the spiderlike fringes, (c) the ATI rings, and (e) the comblike intracycle fringes. To isolate the comblike fringes, the Coulomb field is turned off during the electron propagation process. The corresponding $v_{y,\mathrm{mean}}$ curves are depicted in (b), (d), and (e), respectively. In the inset, the shaded region represents the corresponding electron birth time. (g) The initial phase structure with different directions of the electric field at the electron birth time, extracted from $(2s2p_z)3\sigma_g$ aligned at 45°. The blue (dark gray) curve corresponds to $E(t_r) > 0$, while the yellow (light gray) curve corresponds to $E(t_r) < 0$. Interference patterns are plotted in logarithmic color scale.

Figure 4 displays $v_{y,\mathrm{mean}}$ curves extracted from PMDs for the two tunneling channels from the up- and down-field atoms, respectively, where the tunneling site incorporates a spatial offset from the geometric center of the molecule. It is evident that these two curves exhibit opposite $v_{y,\mathrm{mean}}$ trends. Taking electrons tunneled from the up-field atoms with $v_x > 0$ as an example [see the red (dark gray) line in the regime $v_x > 0$ in Fig. 4], they can either directly leave the molecular ions

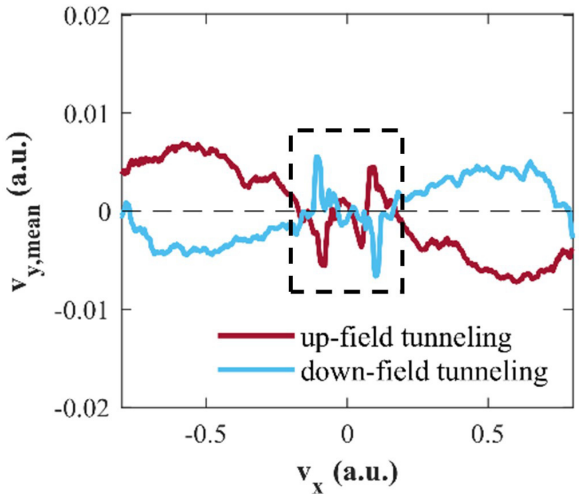

FIG. 4. The $v_{y,\mathrm{mean}}$ curves for up-field [red (dark gray) line] and down-field [light blue (light gray) line] tunneling channels, respectively. The black dashed box frames the reverse structure of the $v_{y,\mathrm{mean}}$ curves in the near-zero-momentum region. Here, the phase structure of tunneling electrons is not concluded.

(i.e., the direct electrons) or go around them before ionization (i.e., the indirect electrons), as illustrated in the simplified trajectory diagrams of Figs. 5(b) and 5(a), respectively. The direct ones are pulled by the upward Coulomb force from the downfield cores, which are attached with a positive shift in the final transverse momentum ($\delta v_y > 0$), and it results in $v_{y,\mathrm{mean}} > 0$; the indirect ones are pulled downward by the downfield cores, attached with a negative δv_y and leading to $v_{y,\mathrm{mean}} < 0$. It was pointed out before that even though the attached δv_y for direct and indirect electrons have opposite signs, only the negative $v_{y,\mathrm{mean}}$ was observed [15]. This is because the indirect ones are subjected to a stronger Coulomb force when they revisit the vicinity of the parent ion and obscure the $v_{y,\mathrm{mean}}$ curve structure from the direct ones. Upon a closer examination of these two $v_{y,\mathrm{mean}}$ curves around $v_x = 0$, however, a subtle inverted TA distribution can be observed, which is highlighted within the dashed box in Fig. 4. Since we ignore the propagation phase ϕ_{pro} of the tunneled electron in the simulation, apparently, this unique structure is masked by the interference fringe-induced oscillating background and has not been extracted in the previous result.

To delve into the underlying dynamics of this unique $v_{y,\mathrm{mean}}$ curve structure, we examined PMDs and the corresponding $v_{y,\mathrm{mean}}$ curves for up-field electrons born in the four adjacent quarter cycles, as shown in Figs. 5(e)–5(h). Their respective typical trajectory diagrams are illustrated in the middle panels of Fig. 5. Given the central symmetry of the PMDs, here we still focus on the region of $v_x > 0$. The PMDs with $v_x > 0$ mainly arise from the superposition of electrons tunneled in the first two quarter cycles, as shown in Figs. 5(e) and 5(f). From the comparison of their extracted $v_{y,\mathrm{mean}}$ curves [see the orange line in Figs. 5(e) and 5(f)], one can clearly identify that they have an opposite $v_{y,\mathrm{mean}}$ but with nearly the same amplitude. This means that the direct electrons also experience a strong Coulomb interaction when they pass by the down-field core, which is contrary to the previous conclusion that the indirect ones always deflected by the asymmetric Coulomb potential more strongly. As a result, the TA of direct electrons should not be covered up by the TA of indirect ones.

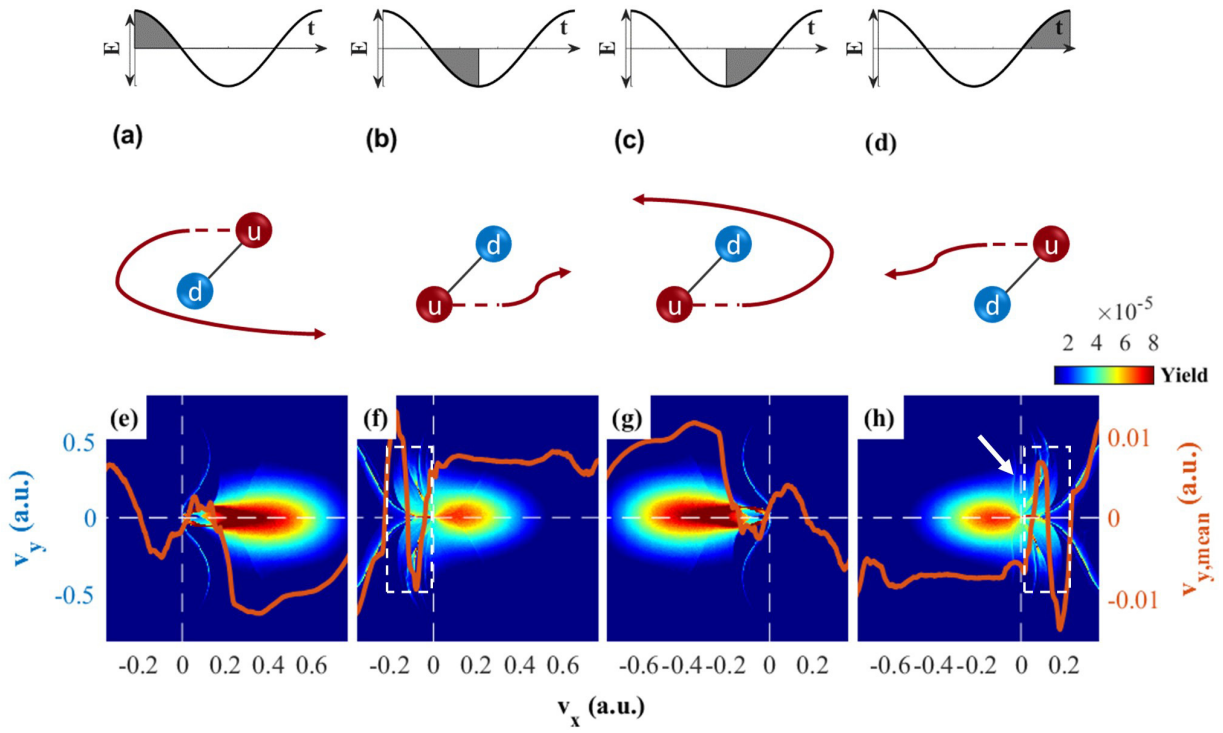

FIG. 5. Separated PMDs of up-field electrons by constraining the birth time of them to individual quarter cycles of the electric field. [(a)–(d)] The simplified trajectory diagrams for the individual quarter cycle. [(e)–(h)] The corresponding PMDs and $v_{y,\mathrm{mean}}$ curves. The white dashed boxes in (f) and (g) indicate the distribution of the prepeak indirect electrons.

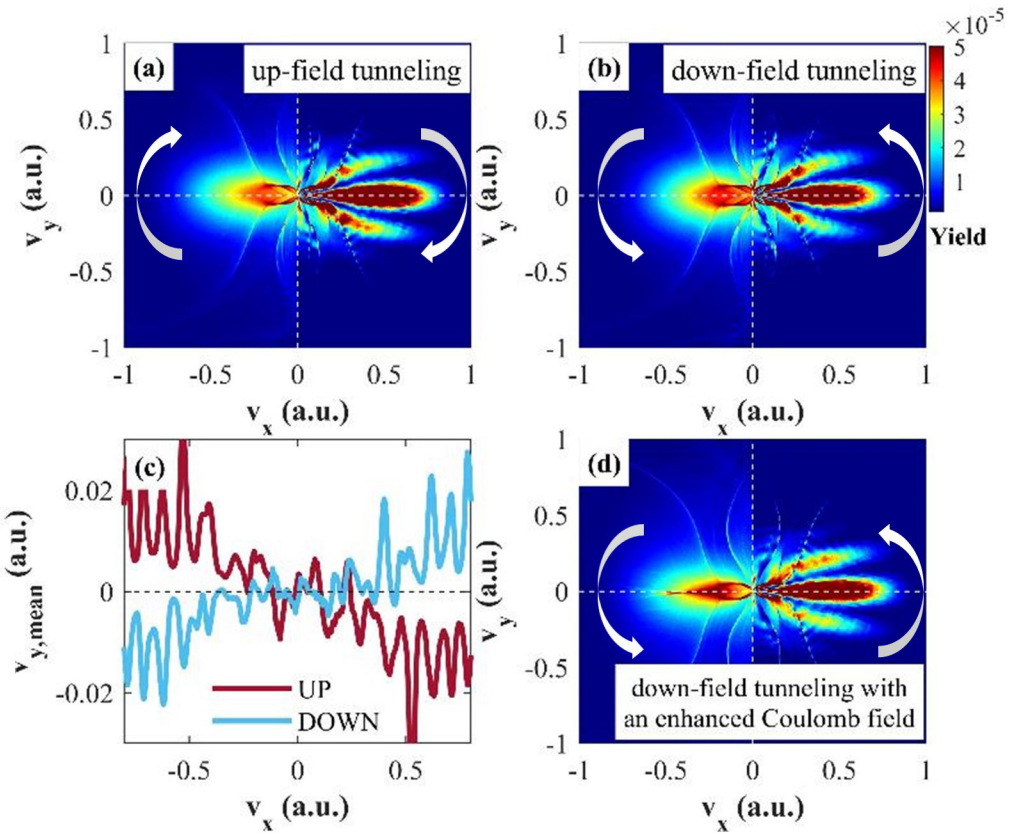

FIG. 6. (a) The PMD of up-field electrons without (left) and with (right) inclusion of the propagation phase. Here only the dominant spiderlike fringes are shown in the right-hand side. White arrows mark the direction of the PMD deflection caused by the asymmetric Coulomb field. (b) Same as (a) but for the electrons tunneled from the down-field atom. (c) The $v_{y,\mathrm{mean}}$ curves corresponding to the PMDs with the inclusion of propagation phase in (a) and (b).(d) Same as (b) but with a 25% enhancement in the intensity of the Coulomb field from the parent ion.

However, the overall TA extracted from the superposition between direct and indirect electrons [i.e., the red (dark gray) $v_{y,\mathrm{mean}}$ curve in Fig. 4] does not compensate for each of them, but has a subtle positive $v_{y,\mathrm{mean}}$ in the near-zero-momentum region and a large negative $v_{y,\mathrm{mean}}$ in the high-energy region in $v_x > 0$. This is because, on the one hand, the direct electrons are always concentrated to a lower energy region because of the Coulomb focusing effect [50], as shown in Fig. 5(f), while the indirect ones distribute in a higher momentum region due to rescattering, as illustrated in Fig. 5(e). They distribute in different momentum regions and give rise to an inversion of the $v_{y,\mathrm{mean}}$ curve. On the other hand, we noticed that not all electrons born before the field maximum within a quarter of a laser cycle can go directly to the detector. A small portion of them could be pulled back to the cores, referred to as the prepeak indirect electrons [see the white dashed box in Figs. 5(f) and 5(h)], which inhibits the $v_{y,\mathrm{mean}}$ curve structure for direct electrons. Specifically, in the $v_x > 0$ region, the distribution of prepeak indirect electrons with $v_{y,\mathrm{mean}} < 0$ in Fig. 5(h) suppresses the $v_{y,\mathrm{mean}}$ curve amplitude of direct electrons in Fig. 5(f) with $v_{y,\mathrm{mean}} > 0$. As a result, one can only observe a relatively small positive $v_{y,\mathrm{mean}}$ around the zero-momentum region in Fig. 4.

In our analysis above, we excluded the phase structure (ϕ_{ini} and ϕ_{pro}) of the EWP to study the asymmetric Coulomb field-induced TA. However, it is crucial to emphasize that the propagation phase ϕ_{pro} is Coulomb potential dependent and the inclusion of ϕ_{pro} will lead to the appearance of the interference patterns in PMDs. When the tunneling EWP propagates in an asymmetric Coulomb field, does the EWP accumulate asymmetric propagation phase structures, leading to a shift in interference fringes? Here we introduce ϕ_{pro} but still disregard ϕ_{ini} in the simulation. The extracted $v_{y,\mathrm{mean}}$ curves for up- and down-field electrons are presented as the red (dark gray) and light blue (light gray) lines in Fig. 6(c), respectively. One can see that although the interference structures overlay the oscillation onto the $v_{y,\mathrm{mean}}$ curves, the $v_{y,\mathrm{mean}}$ curve for the up-field (down-field) electrons still exhibits an overall negative (positive) slope.

To elucidate how the asymmetric Coulomb field modulates interference patterns, we go back to the PMDs of the up- and down-field electrons. Results without and with the inclusion of ϕ_{pro} are shown in the left- and right-hand sides of both Figs. 6(a) and 6(b), respectively. For clarity, only the dominant spiderlike fringes are shown in the right half here. For the up-field electrons without inclusion of ϕ_{pro}, as shown in the left-hand side of Fig. 6(a), they accumulate an asymmetric transverse momentum from the asymmetric Coulomb field. Referring to the extracted $v_{y,\mathrm{mean}}$ curve with a linear negative slope [see the red (dark gray) line in Fig. 4], this suggests a clockwise rotation of the amplitude distribution. After incorporating ϕ_{pro}, the spider fringes emerge, as

shown in the right-hand side of Fig. 6(a). This rotation of the amplitude distribution induced by the asymmetric Coulomb field is manifested in the intensity variations of the spiderlike fringes within different branches. Specifically, the intensity of the lower branch is significantly enhanced because the clockwise rotational amplitude distribution is closer to where it is located. For the down-field electrons, the δv_y can also lead to a rotation of the amplitude distribution, which is counterclockwise as shown in the left-hand side of Fig. 6(b). However, due to the weaker asymmetric Coulomb field experienced by the down-field electrons compared to the up-field ones, its rotation angle is smaller. As a result, it cannot cause a significant change in the intensity of both upper and lower branches of the spiderlike fringes, as observed for the up-field electrons.

One may argue that there could be a ϕ_{pro}-induced shift in the spiderlike fringes, like the pronounced fringe shift caused by the initial phase structure in Fig. 3(a). To confirm the modulation of the fringes by the asymmetric Coulomb field, we enhanced the intensity of the field by 25% for down-field electrons and the obtained PMD is shown in Fig. 6(d). One can easily identify that the upper branch of the spiderlike fringes is significantly enhanced compared to the lower one because of a larger counterclockwise rotation angle of the amplitude distribution. However, Figs. 6(a) and 6(b), even Fig. 6(d), show that all the spiderlike fringes are distributed in their original positions; in other words, under the laser parameters we selected, the wavelength of the scattered EWP is too long to resolve the double-center molecular potential at the equilibrium bond length (2.07 a.u.). Thus, the asymmetric Coulomb field causes the changes in the intensity of the interference fringes rather than the shift of the fringes.

IV. CONCLUSION

In conclusion, our MO-QTMC simulation investigates a system where a linearly polarized laser field interacts with the tilted diatomic molecules. Our study demonstrates that the weighted coefficients of the constituent atomic orbitals for the ionizing molecular orbital have a critical effect on the initial phase structure. This phase structure introduces an additional phase difference between tunneling electrons, leading to the rotation of the spiderlike and comblike fringes while maintaining the structure of the ATI rings. Simultaneously, the asymmetric Coulomb field modulates the amplitude distribution of the PMD, resulting in changes in the intensity of the interference fringes. Apart from the Coulomb-field-induced TA signal for the indirect electrons, we also identified the reverse TA signal for the direct ones with almost the same intensity. We find that the inhibition of TA intensity for direct electrons in the low-energy region is attributed to the fact that some of them are scattered into indirect ones, rather than the result of a weaker Coulomb field they experience.

Furthermore, we uncover distinctions in the mechanisms behind the rotation of spiderlike and comblike fringes by the initial phase structure. The rotation of spiderlike structures originates from the initial phase difference depending on disparities in initial transverse momentum. Such a rotation should be commonly observed in the holograms formed by the interference of scattered electrons (such as spiderlike fringes, fork structures [51], or fishbone structures [52,53]), where a significant initial phase difference will be introduced. However, the rotation of comblike fringes arises from the initial phase difference depending on variations in the direction of instantaneous electric field at the tunnel exit. Since the comblike fringes arise from interference between non-scattered electrons, its initial phase-structure-induced rotation effect exhibits greater potential for extracting electron initial state information in the absence of Coulomb field scattering.

Finally, note that the changes in the intensity of the interference fringes by asymmetric Coulomb field depend on the tunneling sites. This facilitates the future prospect of distinguishing electrons originating from different tunneling sites in PMDs within a holography-compatible manner. Our findings advance the comprehension of photoelectron holograms and expand the potential for utilizing TA to precisely probe the electron dynamics in molecular systems.

ACKNOWLEDGMENTS

This work is supported by the National Key R&D Program of China (Grants No. 2023YFA1407203 and No. 2022YFA1602700), the National Natural Science Foundation of China (Grants No. 12104377 and No. 92250301), the Fundamental Research Funds for the Central Universities (20720220027), Jiujiang Natural Science Foundation Program (S2022KXJJ001), and Natural Science Foundation of Xiamen of China (Grant No. 3502Z20227005).

[1] Y. Huismans *et al.*, Science **331**, 61 (2011).
[2] S. Grundmann, D. Trabert, K. Fehre, N. Strenger, A. Pier, L. Kaiser, M. Kircher, M. Weller, S. Eckart, L. P. H. Schmidt, F. Trinter, T. Jahnke, M. S. Schöffler, and R. Dörner, Science **370**, 339 (2020).
[3] G. Porat, G. Alon, S. Rozen, O. Pedatzur, M. Krüger, D. Azoury, A. Natan, G. Orenstein, B. D. Bruner, M. J. J. Vrakking, and N. Dudovich, Nat. Commun. **9**, 2805 (2018).
[4] M. Han, P. Ge, Y. Shao, M.-M. Liu, Y. Deng, C. Wu, Q. Gong, and Y. Liu, Phys. Rev. Lett. **119**, 073201 (2017).
[5] W. Xie, J. Yan, M. Li, C. Cao, K. Guo, Y. Zhou, and P. Lu, Phys. Rev. Lett. **127**, 263202 (2021).
[6] H. Hetzheim, C. F. d. M. Faria, and W. Becker, Phys. Rev. A **76**, 023418 (2007).
[7] M. He, Y. Li, Y. Zhou, M. Li, W. Cao, and P. Lu, Phys. Rev. Lett. **120**, 133204 (2018).
[8] M. Li, H. Xie, W. Cao, S. Luo, J. Tan, Y. Feng, B. Du, W. Zhang, Y. Li, Q. Zhang, P. Lan, Y. Zhou, and P. Lu, Phys. Rev. Lett. **122**, 183202 (2019).
[9] M. Meckel, D. Comtois, D. Zeidler, A. Staudte, D. Pavičić, H. C. Bandulet, H. Pépin, J. C. Kieffer, R. Dörner, D. M. Villeneuve, and P. B. Corkum, Science **320**, 1478 (2008).
[10] M. Meckel, A. Staudte, S. Patchkovskii, D. M. Villeneuve, P. B. Corkum, R. Dörner, and M. Spanner, Nat. Phys. **10**, 594 (2014).

[11] J. Tan, Q. Ke, D. Wang, X. Hao, J. Xie, G. Yu, X. Xu, and Q. Wu, Phys. Rev. A **108**, 023110 (2023).

[12] S. Eckart, Phys. Rev. Res. **2**, 033248 (2020).

[13] M.-M. Liu, M. Li, C. Wu, Q. Gong, A. Staudte, and Y. Liu, Phys. Rev. Lett. **116**, 163004 (2016).

[14] M.-M. Liu and Y. Liu, J. Phys. B **50**, 105602 (2017).

[15] L. Ortmann, A. AlShafey, A. Staudte, and A. S. Landsman, Phys. Rev. Lett. **127**, 213201 (2021).

[16] T. Zuo and A. D. Bandrauk, Phys. Rev. A **52**, R2511 (1995).

[17] J. Wu, M. Meckel, S. Voss, H. Sann, M. Kunitski, L. P. H. Schmidt, A. Czasch, H. Kim, T. Jahnke, and R. Dörner, Phys. Rev. Lett. **108**, 043002 (2012).

[18] A. Saenz, Phys. Rev. A **61**, 051402(R) (2000).

[19] T. Ergler, A. Rudenko, B. Feuerstein, K. Zrost, C. D. Schröter, R. Moshammer, and J. Ullrich, Phys. Rev. Lett. **95**, 093001 (2005).

[20] A. Staudte, D. Pavičić, S. Chelkowski, D. Zeidler, M. Meckel, H. Niikura, M. Schöffler, S. Schössler, B. Ulrich, P. P. Rajeev, T. Weber, T. Jahnke, D. M. Villeneuve, A. D. Bandrauk, C. L. Cocke, P. B. Corkum, and R. Dörner, Phys. Rev. Lett. **98**, 073003 (2007).

[21] T. Seideman, M. Y. Ivanov, and P. B. Corkum, Phys. Rev. Lett. **75**, 2819 (1995).

[22] E. Constant, H. Stapelfeldt, and P. B. Corkum, Phys. Rev. Lett. **76**, 4140 (1996).

[23] J. Wu, M. Meckel, L. P. H. Schmidt, M. Kunitski, S. Voss, H. Sann, H. Kim, T. Jahnke, A. Czasch, and R. Dörner, Nat. Commun. **3**, 1113 (2012).

[24] K. Codling, L. J. Frasinski, and P. A. Hatherly, J. Phys. B **22**, L321 (1989).

[25] G. Lagmago Kamta and A. D. Bandrauk, Phys. Rev. A **75**, 041401(R) (2007).

[26] G. N. Gibson, M. Li, C. Guo, and J. Neira, Phys. Rev. Lett. **79**, 2022 (1997).

[27] K. Codling and L. J. Frasinski, J. Phys. B **26**, 783 (1993).

[28] K. J. Betsch, D. W. Pinkham, and R. R. Jones, Phys. Rev. Lett. **105**, 223002 (2010).

[29] M. Li, J.-W. Geng, M. Han, M.-M. Liu, L.-Y. Peng, Q. Gong, and Y. Liu, Phys. Rev. A **93**, 013402 (2016).

[30] M. Li, J.-W. Geng, H. Liu, Y. Deng, C. Wu, L.-Y. Peng, Q. Gong, and Y. Liu, Phys. Rev. Lett. **112**, 113002 (2014).

[31] V. I. Usachenko, Phys. Rev. A **73**, 047402 (2006).

[32] T. K. Kjeldsen and L. B. Madsen, Phys. Rev. A **73**, 047401 (2006).

[33] L. D. Landau and E. M. Lifshitz, *Quantum Mechanics* (Pergamon, Oxford, UK, 1977).

[34] N. B. Delone and V. P. Krainov, J. Opt. Soc. Am. B **8**, 1207 (1991).

[35] M. Peters, T. T. Nguyen-Dang, E. Charron, A. Keller, and O. Atabek, Phys. Rev. A **85**, 053417 (2012).

[36] N. I. Shvetsov-Shilovski, M. Lein, L. B. Madsen, E. Räsänen, C. Lemell, J. Burgdörfer, D. G. Arbó, and K. Tőkési, Phys. Rev. A **94**, 013415 (2016).

[37] P. E. Cade and A. C. Wahl, At. Data Nucl. Data Tables **13**, 339 (1974).

[38] X. Lai, R. Sun, S. Yu, Y. Wang, W. Quan, A. Staudte, and X. Liu, Ultrafast Sci. **4**, 0038 (2024).

[39] See Supplemental Material at http://link.aps.org/supplemental/10.1103/PhysRevA.110.013105 for the details of the approximation of HOMO, and the derivation of the initial phase structure, which includes Refs. [5,13,31,32,36–38,40–43].

[40] Z. Y. Lin, X. Y. Jia, C. L. Wang, Z. L. Hu, H. P. Kang, W. Quan, X. Y. Lai, X. J. Liu, J. Chen, B. Zeng, W. Chu, J. P. Yao, Y. Cheng, and Z. Z. Xu, Phys. Rev. Lett. **108**, 223001 (2012).

[41] W. Becker, F. Grasbon, R. Kopold, D. B. Milosevic, G. G. Paulus, and H. Walther, Adv. At. Mol. Opt. Phys. **48**, 35 (2002).

[42] D. B. Milosevic, G. G. Paulus, D. Bauer, and W. Becker, J. Phys. B: At. Mol. Opt. Phys. **39**, R203 (2006).

[43] G. F. Gribakin and M. Y. Kuchiev, Phys. Rev. A **55**, 3760 (1997).

[44] S. Augst, D. D. Meyerhofer, D. Strickland, and S. L. Chin, J. Opt. Soc. Am. B **8**, 858 (1991).

[45] D. D. Hickstein, P. Ranitovic, S. Witte, X.-M. Tong, Y. Huismans, P. Arpin, X. Zhou, K. E. Keister, C. W. Hogle, B. Zhang, C. Ding, P. Johnsson, N. Toshima, M. J. J. Vrakking, M. M. Murnane, and H. C. Kapteyn, Phys. Rev. Lett. **109**, 073004 (2012).

[46] D. G. Arbó, K. L. Ishikawa, E. Persson, and J. Burgdörfer, Nucl. Instrum. Methods Phys. Res., Sect. B **279**, 24 (2012).

[47] P. Agostini, F. Fabre, G. Mainfray, G. Petite, and N. K. Rahman, Phys. Rev. Lett. **42**, 1127 (1979).

[48] K. Lin, S. Eckart, A. Hartung, D. Trabert, K. Fehre, J. Rist, L. P. H. Schmidt, M. S. Schöffler, T. Jahnke, M. Kunitski, and R. Dörner, Sci. Adv. **8**, 7386 (2022).

[49] A. S. Maxwell and C. F. d. M. Faria, J. Phys. B **51**, 124001 (2018).

[50] T. Brabec, M. Y. Ivanov, and P. B. Corkum, Phys. Rev. A **54**, R2551 (1996).

[51] M. Möller, F. Meyer, A. M. Sayler, G. G. Paulus, M. F. Kling, B. E. Schmidt, W. Becker, and D. B. Milošević, Phys. Rev. A **90**, 023412 (2014).

[52] X.-B. Bian and A. D. Bandrauk, Phys. Rev. Lett. **108**, 263003 (2012).

[53] M. Haertelt, X.-B. Bian, M. Spanner, A. Staudte, and P. B. Corkum, Phys. Rev. Lett. **116**, 133001 (2016).